4938 *Biochemistry* **1999,** *38,* 4938−4947

Solution Structures of Dimeric Kinesin and *Ncd* Motors[†]

Deborah B. Stone,[‡] Rex P. Hjelm, Jr.,[§] and Robert A. Mendelson*,[‡]

Cardiovascular Research Institute and Department of Biochemistry and Biophysics, University of California, San Francisco, California 94143-0130, and Los Alamos Neutron Scattering Center, Los Alamos National Laboratory, Los Alamos, New Mexico 87545

Received October 5, 1998; Revised Manuscript Received February 12, 1999

ABSTRACT: The dimeric structure of the members of the kinesin family of motor proteins determines the individual characteristics of their microtubule-based motility. Crystal structures for *ncd* and kinesin dimers, which move in opposite directions on microtubules, show possible states of these dimers with ADP bound but give no information about these dimers in solution. Here, low-angle X-ray and neutron scattering were used to investigate their solution structures. Scattering profiles of *Drosophila ncd* 281−700 (NCD281) and human kinesin 1−420 (hKIN420) were compared with models made from the crystallographically determined structures of NCD281 and rat kinesin 1−379 (rKIN379). From the low-angle region it was found that the radius of gyration (R_g) of NCD281 is 3.60 ± 0.075 nm, which is in agreement with the crystallography-based model. Scattering by longer *ncd* constructs (NCD250 and NCD224) is also well fit by the appropriate crystallography-based models. However, the measured R_g of hKIN420, 4.05 ± 0.075 nm, is significantly smaller than that of the crystallography-based model. In addition, the overall scattering pattern of NCD281 is well fit by the model, but that of hKIN420 is poorly fit. Model calculations indicate that the orientation of the catalytic cores is different from that observed in the rKIN379 crystal structure. Like the crystal structure, the best-fitting models do not show 2-fold symmetry about the neck axis; however, their overall shape more resembles a mushroom than the "T"-like orientation of the catalytic cores found in the crystal structure. The center of mass separations of the catalytic cores in the best-fitting models are 0.7−1 nm smaller than in the crystal structure.

Kinesin-like microtubule-based motors play diverse roles in biology ranging from organelle transport (kinesin) to chromosomal segregation in meiosis and mitosis (nonclaret disjunctional protein or *ncd*) to the transport of substances needed for neuronal cell differentiation (*unc* 104). The mechanism by which such motors move along microtubule "tracks" while catalyzing the hydrolysis of ATP is largely unknown (for recent reviews see refs *1* and *2*). *Ncd* and kinesin, the motors studied here, have two heavy chains which are composed of distinct structural regions. At the proximal end of the paired heavy chains are two ∼320 amino acid globular "catalytic core" domains which possess ATP and microtubule binding sites. These catalytic cores are joined to a class-specific coiled-coil 10−40 amino acid "neck" domain (*3−5*) which together with the catalytic core domains may be direction and velocity determining. A portion or all of the neck may be a coiled coil. The neck is, in turn, joined to a long coiled-coil "stalk". At the distal end of the stalk, at least for kinesin, are two cargo-carrying light chains. These modules may be arranged with the catalytic core domain at the NH_2 terminus (e.g., conventional kinesins) or the COOH terminus (*ncd*) of the polypeptide chain. In the former case, motor proteins move toward the rapidly growing "plus" end of microtubules; in the latter case, movement is directed toward the minus end. Isolated catalytic core domains from plus- and minus-end-directed motors share 41% sequence homology and similar crystal structures (*6, 7*). They also display similar kinetic parameters for the ATPase cycle (*8, 9*) and bind to microtubules with similar orientations (*10−12*). Recently, the crystal structures of truncated dimers of rat kinesin 1−379 (rKIN379)[1] (*13*) and *Drosophila ncd* 281−700 (NCD281) (*5*) have become available, and they show remarkably different dispositions of the catalytic core domains. This difference has been postulated to account for the differing directionality of these two motors (*5*).

In an earlier neutron scattering study on microtubule-based motor proteins (*14*), we found that the solution structures of the monomeric catalytic cores of *Drosophila ncd* and human kinesin were very similar. Herein, we report a study of the solution structures of dimeric constructs of NCD281 and human kinesin 1−420 (hKIN420) by low-angle X-ray and neutron scattering. This method allows us to test whether the crystallographic structures are valid in solution. A rationale for such studies is that the contacts between motor

---

[†] This work was supported by University of California Office of the President UCDRD and CULAR grants to R.A.M. and R.P.H. and by NIH Grant P01-AR42895 to R.A.M.

* To whom correspondence should be addressed.

[‡] University of California, San Francisco.

[§] Los Alamos National Laboratory.

[1] Abbreviations: EM, electron microscopy; M_r, molecular weight; mant, *N*-methylanthraniloyl; *ncd*, nonclaret disjunctional protein from *Drosophila*; *Q*, the momentum transfer, defined as $Q \equiv 4\pi \sin \theta/\lambda$, where 2θ is the scattering angle and λ is the neutron or X-ray wavelength; R_g, radius of gyration; TLCK, *N*α-*p*-tosyl-L-lysine chloromethyl ketone. We denote bacterially expressed kinesin and *ncd* constructs by originating species with a lower case character when required, followed by NCD or KIN, followed by a numeral which specifies the relevant terminal residue number. Thus rat kinesin 1−379 is rKIN379 and *Drosophila ncd* 281−700 is NCD281, etc.

10.1021/bi982374z CCC: $18.00

cores of the dimer seen in the rKIN379 crystal structure are tenuous and between nonconserved residues; it is possible that packing forces in the crystal play a role in the observed orientations of the catalytic cores. We find that the scattering pattern for NCD281 can be well accounted for by the dimer crystal structure plus missing residues in the catalytic core and neck; however, hKIN420 scattering cannot be fit in a similar way. We attribute this to a difference in the orientation of the kinesin catalytic cores between solution and the crystal.

EXPERIMENTAL PROCEDURES

Expression and Purification of Ncd Dimers. Drosophila ncd dimers were prepared by a modification of the method used previously for the purification of *the ncd* catalytic core (*14*). The recombinant plasmid pHB40P-*ncd* containing the truncated *ncd* gene E224-K700, D250-K700, or E281-K700 was transformed into BL21(DE3)pLysE host cells (*15*). Induction was carried out with 0.2 mM IPTG. Frozen cell pellets were suspended in buffer A (10 mM PIPES, pH 7.2, 80 mM NaCl, 2 mM $MgCl_2$, 1 mM EGTA, 1 mM DTT, and 5× protease inhibitors) and lysed in the presence of 0.1% Triton X-100 using 1 mg of lysozyme/mL with homogenization in a 40 mL Wheaton Dounce tissue grinder. (The 1× protease inhibitor cocktail used throughout consisted of 1 mg/L chymostatin, 1 mg/L leupeptin, 1 mg/L pepstatin, 1 mg/L aprotinin, and 5 mg/L TLCK.) Following incubation with 0.1 mg/mL DNase and 10 mM $MgCl_2$ for 20 min, the cell lysate was centrifuged at 245000*g* for 60 min at 4 °C. Dimer protein was purified from the cell supernatant by gradient chromatography on Pharmacia S-Sepharose FF followed by passage through *Q*-Sepharose HP in a buffer similar to buffer A but containing 12 mM Tris-HCl at pH 7.6 and 1× protease inhibitors. A final gel filtration purification step was carried out on Sephacryl S-300 HR in 25 mM PIPES, pH 7, 200 mM NaCl, 1 mM $MgCl_2$, 0.5 mM EGTA, 0.5 mM DTT, 20 μM MgATP, and 1× protease inhibitors (buffer B). Purified *ncd* dimers were dialyzed against buffer B containing 50% glycerol and 0.1 mM MgATP and stored at −15 °C. The ATPase rate of all *ncd* dimers in a 50 mM Pipes, pH 7, 200 mM NaCl, 2 mM $MgCl_2$, 1 mM EGTA, 1 mM DTT, 5 mM MgATP buffer at 25 °C was 0.01 s^{-1} catalytic $core^{-1}$. This rate was 3 times the *ncd* monomer rate on a per-head basis. With 98% D_2O present the ATPase was unchanged within error.

Expression and Purification of Kinesin Dimers. A truncated human conventional kinesin consisting of residues M1−K420 was cloned into the pET17b expression vector and expressed in *Escherichia coli* strain BL21(DE3)pLysE (Shimizu, Thorn, Ruby, and Vale, manuscript in preparation). Cells were grown overnight in TPM-ampicillin (*16*) at 33 °C without chemical induction. Frozen cell pellets were suspended in buffer C (25 mM PIPES, pH 6.8, 2 mM $MgCl_2$, 1 mM EGTA, 1 mM DTT, and 5× protease inhibitors), containing 100 mM KCl, then lysed, and centrifuged as described for *ncd*. The cell supernatant was loaded onto a phosphocellulose column (Whatman International Ltd.), prepared according to the manufacturer's directions, and equilibrated in buffer C containing 100 mM KCl. Following elution with a 0.1−1.0 M KCl gradient, fractions containing hKIN420 were pooled and dialyzed against buffer C containing 100 mM KCl. The dialyzed pool was then applied to an S-Sepharose HP column in series with a *Q*-Sepharose HP column equilibrated in buffer C containing 100 mM KCl and 1× protease inhibitors. After washing, the S-Sepharose HP column was disconnected and hKIN420 was eluted with a 0.1−0.4 M KCl gradient in buffer C. The final purification step and storage were done as for *ncd*. The ATPase rate of hKIN420 was 0.03 s^{-1} catalytic $core^{-1}$ under the same buffer conditions as used for *ncd* monomers and dimers.

Biochemical Methods. ATPase activities of *ncd* and kinesin dimers were measured colorimetrically (*17*). Protein concentrations were determined spectrophotometrically using extinction coefficients calculated from the amino acid composition (*18*) and including 1 mol of ADP per single chain. The following values were used for $A^{0.1\%}{}_{280}$: NCD224, 0.535 cm^{-1}; NCD250, 0.566 cm^{-1}; NCD281, 0.605 cm^{-1}; hKIN420, 0.835 cm^{-1}.

Scattering Measurements. Samples were transported to the experimental site on ice in the 50% glycerol storage buffer (see above) contained in a dialysis bag surrounded by storage buffer. After dialysis against the experimental solvent, the samples were spun at 245000*g* for 90 min in order to remove any remaining aggregates. Samples were maintained at 4−6 °C until being loaded into the scattering cells.

Neutron scattering measurements were carried out at the Manuel Lujan, Jr., Neutron Scattering Center spallation source (LANSCE, Los Alamos National Laboratory, Los Alamos, NM) on the Low-*Q* Diffractometer and at the NIST (Gaithersburg, MD) reactor on the 30m NG3 beamline. Samples at each protein concentration were placed in 2 mm path-length quartz optical cuvettes. The cuvettes were placed in automatic sample changers and held at 6−10 °C throughout the course of the measurements.

X-ray measurements were carried out at the Stanford Synchrotron Radiation Laboratory (SSRL, Stanford, CA) on beamline 4-2 using a Xe−CO_2 filled linear detector as employed previously (*19*). The X-ray energy was set at 8900 eV by a Si(111) crystal monochromator, and the sample-to-detector distance was 2.096 m. Routine position calibrations were made using a sealed cholesterol myristate sample (*20*). The sample was maintained at 18.5 °C in a 1.2 mm path-length (flat) cell having cleaved mica windows. Concentration series were run sequentially in the same cell, going progressively from the lowest to the highest protein concentration. Sample cross-contamination was prevented by washing the sample cells with many changes of buffer between samples and by using different cells for *ncd* and kinesin. The protein concentration of each sample was determined after the measurement. Counting rates were always maintained below 15 000 s^{-1} to minimize distortion due to electronic pulse pileup and space charge effects in the detector. Analysis of (60 s) time dumps of scattering data revealed no detectable radiation or temperature damage for at least 1200 s. Nevertheless, the total sample exposures were 600 s or less for data included in this study. All scattering data for both *ncd* and kinesin dimer were accumulated during the same data collection period and as close in time as possible.

Scattering Data Analysis. Reactor neutron and X-ray data were reduced using the laboratory-developed programs SCATMAN and SSRLANA, which corrected all scattering curves for detector response and dead time. At the LANSCE spallation source, data were collected both as a function of position on an area detector and as a function of neutron time of flight after the initiating proton pulse. Since Q, the momentum transfer, depends on both the wavelength (λ) and scattering angle (2θ) via the relation $Q \equiv 4\pi \sin(\theta)/\lambda$ and since λ depends on the time of flight, both parameters and their precision must be taken into account when constructing a histogram of $I(Q)$ vs Q (*21*). From convoluting model scattering curves with experimental parameters, we found no differences in the expected $I(Q)$ vs Q using a bin width of 100 $\Delta Q/Q$ = 1.5% and 5% rms. Since the larger bins increased the statistical accuracy of $I(Q)$, the latter bin width was employed.

The radius of gyration (R_g) was extracted from low-Q data by means of the Guinier approximation:

$$I(Q) \approx I(0) \exp(-Q^2 R_g^{\,2}/3) \tag{1}$$

Here $I(0)$, the scattering intensity extrapolated to $Q = 0$, is proportional to the molecular weight times the protein concentration (C). R_g and $I(0)$ were obtained by least-squares fits to Guinier plots (ln [$I(Q)$] vs Q^2).

Modeling of Scattering Data. Modeling of kinesin dimer structures was done as follows. The complete starting model was aligned so that the long axis of the neck was coincident with the z-axis. For cases in which the starting model was a dimer, one catalytic core was deleted from the aligned PDB file. The origin of the coordinate system was then moved to the C_α of Thr^{338} of the remaining catalytic core, which is located at the transition point between the neck and the catalytic core moieties. A rigid-body rotation through Euler angles (ϕ_1, θ_1, ψ_1) was then applied to atoms in the catalytic core only.[2] The coordinate system was next moved back to the neck axis, and a second catalytic core was generated by a polar rotation (θ_{neck}) of the atoms of the first catalytic core around the neck axis. In one case the second catalytic core was generated using $\theta_{neck} = 180°$ followed by rotations about the second pivot point through another set of Euler angles (ϕ_2, θ_2, ψ_2). This increased the number of geometric parameters specifying the model dimer from four to six. Other fits were made with imposed 2-fold symmetry ($\theta_{neck} = 180°$; $\phi_1 = \phi_2$, $\theta_1 = \theta_2$, $\psi_1 = \psi_2$) or by leaving the first catalytic core fixed ($\phi_1 = \theta_1 = \psi_1 = 0$) and rotating the other or by only varying θ_{neck}.

Global least-squares searches over a coarse grid were performed by exploring all of parameter space in 30° steps. Minima were selected manually from a list of parameters sorted by increasing χ_ν^2. The parameters at these minima were refined by rocking about these positions in 10° steps, moving to the new minima, and rocking again until no further improvement in χ_ν^2 was achieved. The parameter step size was then halved and the process repeated. To minimize computation time, scattering curves were only calculated when the model R_g was between 3.85 and 4.6 nm. Also scattering curves were not recomputed if the new model-determining rotation matrices were identical to previous ones. The final step size in all parameters was 2.5°.

Scattering curves were computed from the PDB files using the programs CRYSOL (*23*) and CRYSON (*24*) for X-ray scattering and neutron scattering, respectively. These programs utilize a method which accounts for excluded molecular volume of solvent and in addition allows for scattering by an interface of water having a slightly different density than bulk solvent. Here 15 spherical harmonics defined the shape of the molecule. These programs were used either in a stand-alone mode for direct comparison of scattering data with predictions from crystallographic dimer structures or as a callable module of the larger least-squares modeling routine described above. Although all fitting was done in reciprocal space, scattering data and best-fitting model intensities were also Fourier transformed to generate the distribution of molecular chords [$P(r)$] for data and best-fitting models using the program GNOM (*25*).

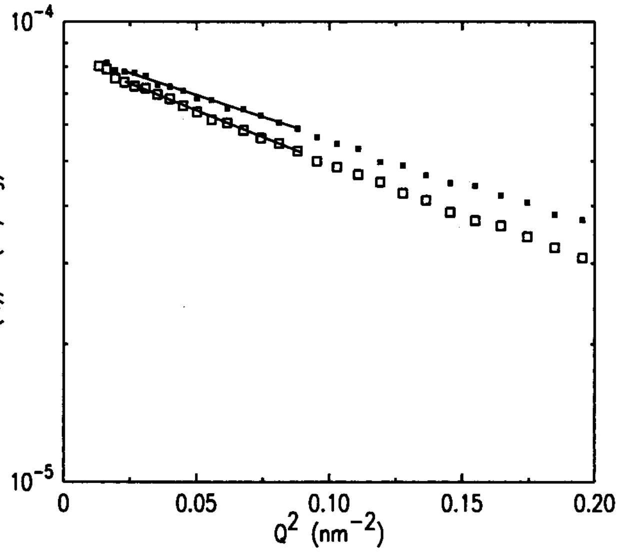

FIGURE 1: Guinier plots of X-ray scattering data by hKIN420 (□) and NCD281 (■) dimers with bound MgADP. The solid lines are least-squares fits of eq 1 over the range $0.02 < Q^2 < 0.088$ nm^{-2}. The solvent contained 50 mM Pipes, pH 7, 250 mM NaCl, 2 mM $MgCl_2$, 1 mM EGTA, 1 mM DTT, 0.1 mM ADP (hydrolyzed ATP), and protease inhibitors. The NCD281 concentration was 2.4 mg/mL and the hKIN420 concentration was 6.5 mg/mL.

For both X-rays and spallation-source-generated neutrons, it was demonstrated by convolution (*21, 25*) of typical model curves with experimental parameters that the use of experimental data without convolution negligibly affected models and R_g. This was also true for R_g determination by reactor-generated neutrons.

RESULTS

Low-Q Data. Initial neutron scattering experiments on samples in solvents containing 100−500 mM NaCl indicated that it was necessary to have at least 200 mM salt present to maintain sufficient solubility at high protein concentrations. Similar results have been found by others (*26*) using hydrodynamic methods. Typical Guinier plots for X-ray scattering by hKIN420 and NCD281 (with bound MgADP) in 250 mM NaCl are shown in Figure 1. The concentration dependencies of the observed R_g and $I(0)/C$ derived from such plots by fitting eq 1 are shown in Figure 2 for X-ray (250 mM NaCl) and neutron (200 mM NaCl) scattering experiments. In contrast to X-ray data, neutron data for both *ncd* and kinesin show a positive slope for R_g vs C. Further, the slopes of $I(0)/C$ vs C are not equivalent for the two proteins as they are in the X-ray data. The neutron and X-ray data were taken with slightly different NaCl concentrations.

---

[2] The notation of Goldstein (*22*) is used throughout for Euler angles.

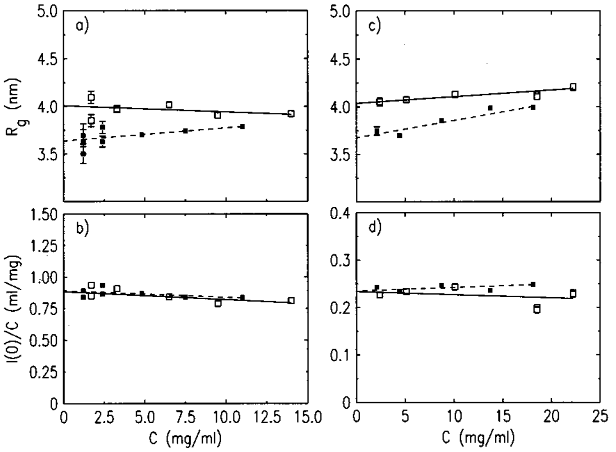

FIGURE 2: Concentration dependence of scattering results from the low-Q region (see Figure 1). R_g and $I(0)/C$ were determined by fitting Guinier plots (Figure 1) over the range $0.02 < Q^2 < 0.088$ nm^{-2}. Data points for hKIN420 (□) and NCD281 (■) dimers are shown. Straight-line fits to the concentration dependence were weighted by counting statistics only. (a) Concentration dependence of the observed R_g determined from X-ray scattering data. (b) Concentration dependence of the observed $I(0)/C$ determined from X-ray scattering data. (c) Same as (a) but the data are from neutron scattering experiments. The 99% D_2O solvent used in neutron experiments contained 50 mM Pipes, pH 7, 200 mM NaCl, 2 mM $MgCl_2$, 1 mM EGTA, 1 mM DTT, protease inhibitors, and 0.1 mM ADP (hydrolyzed ATP). (d) Same as (b) but the data are from neutron scattering experiments.

In addition to this fact, the observed slope differences could also arise from association effects induced by D_2O. Despite these differences in slope, kinesin and *ncd* dimers give almost the same extrapolated absolute R_g values from X-ray and neutron data.[3] Also, $I(0)/C$ values extrapolated to $C = 0$ are virtually identical for both proteins in both neutron and X-ray scattering experiments. Since $I(0)/C$ is proportional to molecular weight and since NCD281 and hKIN420 have virtually the same molecular weights (but not the same mass distribution), this is the expected result. In particular, the invariance of the extrapolated $I(0)/C$ indicates that the fitting region employed is adequate to determine the correct R_g of kinesin, which has a greater fraction of its mass in the neck plus stalk, and a greater R_g. Other experiments (not shown) using myosin S1 ($M_r = 131\,000$), sweet potato β-amylase ($M_r = 201\,000$), and in some cases H_2O (for neutrons) as standards gave the correct molecular weights of NCD281 and hKIN420 within an estimated error of 10%.

In addition to comparing the R_g's of hKIN420 and NCD281, we have measured the scattering from NCD250 and NCD224 (Figure 3), which are *ncd* constructs having longer stalks. These molecules show significant curvature in the region where NCD281 is linear, indicating that their true Guinier region, reflecting the increased M_r, occurs in a lower Q^2 range.

Fits to Scattering Patterns Using Crystallographic Results. For monodisperse particles, randomly distributed in solution, scattering patterns are determined by the distribution of interatomic chords within the scattering particles. Thus, one can test models of the scattering molecule by computing its scattering pattern from a given structure.[4]

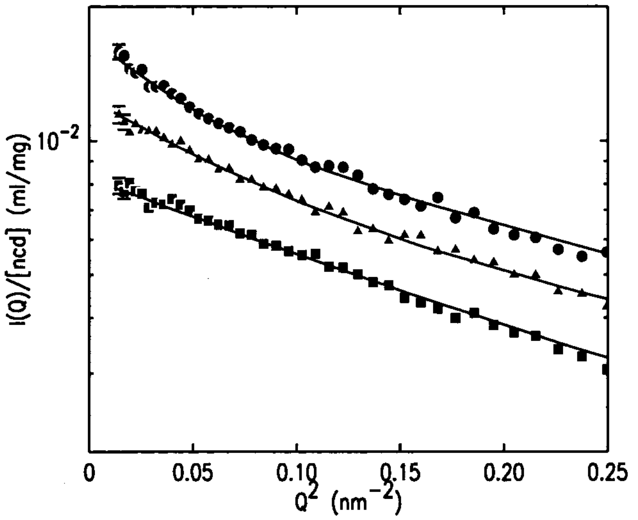

FIGURE 3: Typical Guinier plots of neutron scattering by *ncd* dimers having different lengths. The filled circles (●) are scattering from NCD224, the filled triangles (▲) are scattering from NCD250, and the filled squares (■) are from NCD281. The solid lines are computed scattering curves from dimers consisting of the crystallographic NCD281 structure (*5*) with appropriate lengths of coiled-coil rod added to yield the correct M_r. NCD250 and NCD281 intensities have been multiplied by 0.75 and 0.5, respectively, for display purposes. The increasing curvature at low Q^2 with increasing M_r is a result of the increasing maximum chord ($d_{max} = 13.6$, 18.3, and 21.9 nm, for NCD281, NCD250, and NCD224 respectively), which moves the true Guinier region to progressively lower Q^2. The protein concentrations were 10−12 mg/mL. The 99% D_2O solvent contained 50 mM Pipes, pH 7, 250 mM NaCl, 2 mM $MgCl_2$, 1 mM EGTA, 1 mM DTT, protease inhibitors, and 0.1 mM ADP (hydrolyzed ATP).

We have compared the computed scattering from the crystallographically determined NCD281 structure (2NCD) with our NCD281 scattering data and the computed scattering from the crystallographically determined structure (3KIN) of rKIN379 with our scattering data from hKIN420. Because of the 87% sequence identity of rat and human kinesin (*28*), it is likely that hKIN420 and rKIN379 have the same low-resolution structure. Both rKIN379 and NCD281 crystallographic structures are missing portions of the stalk and some residues in the catalytic core domain. Thus, to more accurately compute the expected scattering patterns, it was necessary to add these residues to the structures.

For *ncd* dimers there are 38 missing residues in each of the catalytic cores of the crystal structure (2NCD; *5*). In the case of NCD281 these missing residues represent 9% of the total mass. The missing residues in loop 11 (residues 588−597) and the C-terminus (residues 673−700) are on opposite sides of the catalytic core. Their absence could affect the scattering pattern, as they might project out from the bulk of each catalytic core's mass. We performed model calculations on NCD281 both with and without added catalytic core residues. For loop 11 half of the residues were added at each end; for the C-terminus, all were added to the last known

---

[3] On the basis of model calculations, the neutron R_g's should be about 0.07 nm lower than the X-ray R_g's due to the contrast difference. This assumes equivalent experimental conditions and little or no D_2O exchange. This difference is within the error of the measurements.

[4] By a spherical Fourier transformation of the intensity one can also compute the chord distribution directly. However, technical limitations on estimation of the magnitude of the maximum chord (*27*), which is a parameter in the transformation, dictate that fitting of models be done in reciprocal space.

Table 1: Radii of Gyration of Kinesin and *Ncd* Dimers

	R_g X-rays[a] (nm)	R_g neutrons[a] (nm)	$R_g^{\text{in vacuo}}$ crystal-based model[b] (nm)	R_g^{hydrated} crystal-based model[b,c] (nm)	$d_{\max}$ crystal-based model[b,d] (nm)	d_{sep} crystal-based model[b,e] (nm)	χ_ν^2
NCD281	3.60 ± 0.075	3.65 ± 0.13	3.55/3.47	3.73/3.72	13.6/13.6	4.75/4.50	1.03/0.93
hKIN420	4.05 ± 0.075	4.10 ± 0.13	4.49/4.50/4.53	4.64/4.65/4.66	16.1/16.1/16.1	6.09/6.19/6.26	5.01/5.22/5.21

[a] Includes results from experiments in addition to those shown in Figure 2. [b] $R_g^{\text{in vacuo}}$ is the electronic R_g computed from the atomic coordinates using all atoms in a given PDB file. The first values given are without readdition of the residues missing in the catalytic cores of the crystal structure. The second values have residues readded at the available loop ends (and at the C-terminus for NCD281) as described in the text. For hKIN420 the third set of values is derived when the loop 11 structure given in ref *6* is included. This extended loop, whose structure was not determined experimentally, is probably distributed about the given position in solution. Thus the structural parameters derived from its inclusion are likely an upper limit on what would be expected. [c] Computed from X-ray results using CRYSOL with a 0.3 nm water shell; best fits were obtained using $\rho = 88$ e/nm^3 and $r_{\text{av}} = 0.158-0.165$ nm. [d] $d_{\max}$ is the longest chord in the molecule. [e] d_{sep} is the center-of-mass to center-of-mass separation of the catalytic cores.

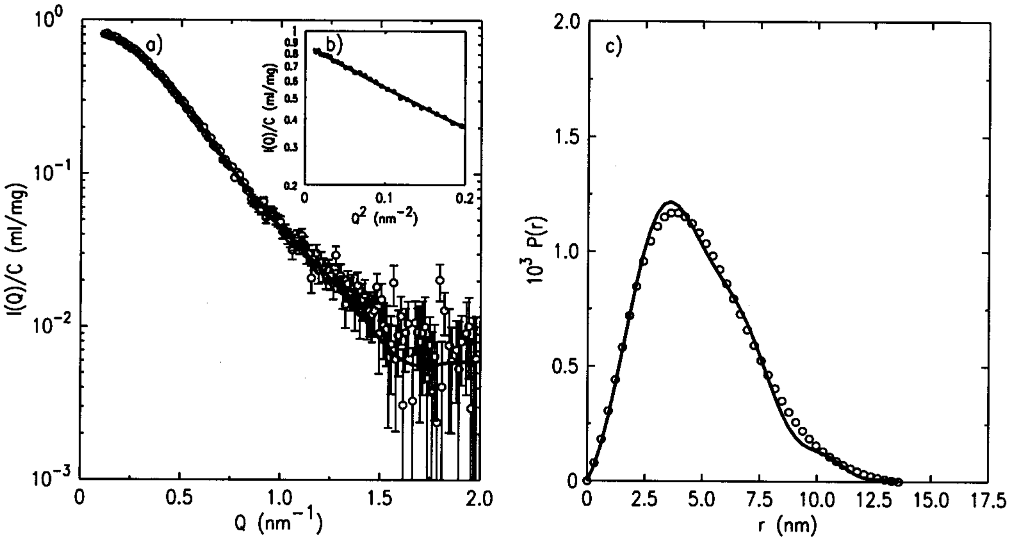

FIGURE 4: X-ray scattering by NCD281 (as in Figure 1). (a) Plot of observed intensity vs Q. The solid line is a fit computed from the 2NCD crystallographic structure (*5*) with added residues in the catalytic cores (see text) and the stalk. Open circles are data (as in Figure 1). The fitting range was $0.1 < Q < 2$ nm^{-1}. (b) Guinier plot of the same data and model as in (a). (c) Chord distributions [$P(r)$] obtained by Fourier transforming the scattering data in (a) and the calculated scattering by the crystallography-based structure (solid line).

residue. In addition, coiled-coil stalk residues were added to give the appropriate M_r. As can be seen in Table 1, there was a relatively small effect on both the observed R_g and the χ_ν^2 values of the *ncd* fits. The fits to the experimental R_g of NCD281 (Table 1, Figures 2 and 3) and scattering patterns (Figure 4) are good ($\chi_\nu^2 \approx 1$), and one can be confident that the low-resolution solution structure resembles that obtained by crystallography when the missing residues in the stalk are included. We note, however, that the crystallographic $P(r)$ shows a small ripple which is not seen in the data. This absence could be indicating that the average position of the missing C-terminal residues is closer to the opposite catalytic core than the last known C-terminal residue—so that the space between the cores is more nearly filled in.

The fits to the longer ncd dimers (Figure 3), NCD250 and NCD224, are also noteworthy. The fits obtained at low Q are good and indicate that the stalk portions of these constructs are well described by coiled coils of increasing length. This is in agreement with secondary structure predictions for coiled coils by the program COILS (and COILS2) (*29*) which predicts that the region of *ncd* between residues 200 and 340 is likely to be a coiled coil.

On the other hand, the fit of a model consisting of the rKIN379 crystal structure plus missing core and stalk residues to hKIN420 scattering data (Figure 5) is poor ($\chi_\nu^2 \approx 5$), and the model R_g is much larger than experimentally observed (Table 1). This result does not depend significantly on whether the 17 missing loop 11 residues (4% of the total mass) in each of the 3KIN catalytic cores are readded at the end of the ends of the loop, are modeled using the loop proposed in the monomer crystallography (*6*), or are not readded (Table 1). The $P(r)$ plots of kinesin (Figure 5c) are dramatically different from those of *ncd* (Figure 4c), reflecting a greater separation of the catalytic core domains and the greater length of the molecule. The simplest interpretation of the difference between the hKIN420 data and rKIN379-derived model plots is that the catalytic core separation d_{sep} (reflected in the bump near 6−7 nm in Figure 5) is smaller and the overall length of the molecule is shorter than that of the model.

Modeling the Structure of the Kinesin Dimer. As the scattering by the *ncd* dimers is well fit by models comprised of the crystallographic structure plus added stalk, such models are likely to be accurate representations of the structures of *ncd* dimers in solution. On the other hand, hKIN420 was poorly fit by the crystallographic structure of rKIN379 plus added residues. There are a number of reasons why this could be so.

First, an examination of the crystal contacts for 3KIN suggests that the packing of kinesin in the crystal could set the kinesin catalytic core orientation. Each catalytic core makes three to four times as many contacts with symmetry-

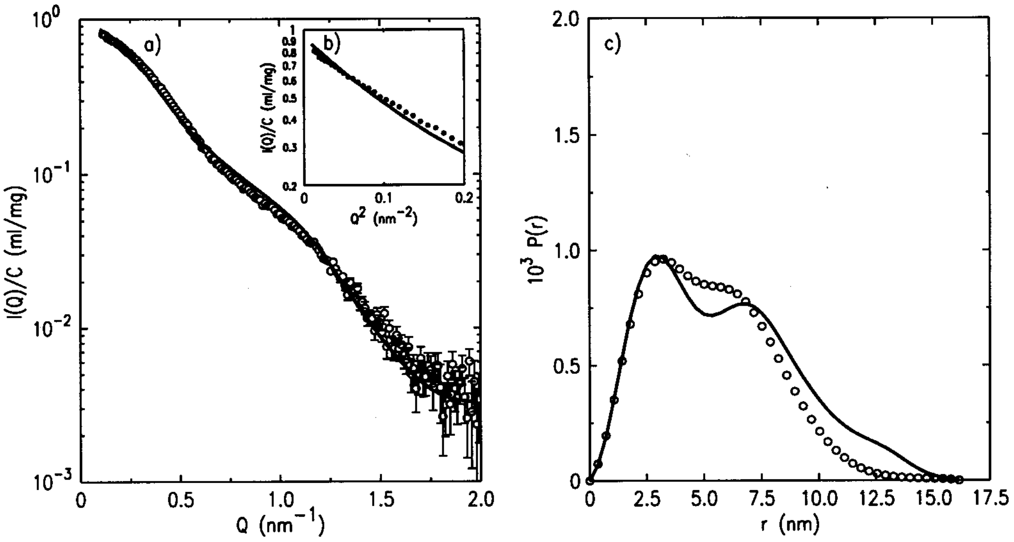

FIGURE 5: X-ray scattering by hKIN420. (a) Plot of observed intensity vs Q. The solid line is a fit computed from the 3KIN crystallographic structure with added residues in the catalytic cores (half of the missing residues added at each end of the loop) and the neck and stalk. Open circles are data (as in Figure 1). The fitting range was $0.1 < Q < 2$ nm^{-1}. (b) Guinier plot of the same data and model as in (a). (c) Chord distributions [$P(r)$] obtained by Fourier transforming the scattering data in (a) and the calculated scattering by the crystallography-based structure.

related mates as with the partner catalytic core. The interchain interactions in 3KIN appear to be primarily between the (nonconserved) charged surface residues Lys^{160} and Glu^{221} (*13*). Also, other possible interchain interactions may occur between the (partially conserved) Asp^{3} in *one* of the catalytic cores and the (partially conserved) Lys^{354} in the neck region of the other chain (*30*).

Second, the hKIN420 studied here is longer than that used in crystallographic studies and is from a different species. The longer kinesin construct used here was chosen to mitigate concerns about the aggregation reported for shorter dimers (*26, 31*), and it is known (R. Vale, personal communication) that this construct exhibits "processivity" or the ability to remain attached to MTs while exhibiting motility. Discounting the species difference, which seems likely to be negligible on the basis of sequence identity, there is a possibility that the stalk of kinesin is bent or bends near residue 375. Secondary structure predictions and peptide experiments (*4*) suggest that there is little or no α-helix in the residue 370−383 region and perhaps somewhat beyond.[5] However, there is no direct evidence of a bend or bending. Shadowing micrographs (*32*) of native bovine kinesin only indicate a bendable region about 35 nm from the near edge of the catalytic cores. A bend located near residue 375 would be about 8 nm from the near edge of the catalytic cores. Finally, the possibility exists that the catalytic cores are in some way disordered and this disordering is responsible for the difference between the crystal structure-based model and experimental results.

We investigated the possibility that a bent stalk alone could account for our scattering data. Least-squares searches allowing the stalk of the rKIN379 plus missing residues model to bend at residue 375 through various Euler angles to achieve a best fit to the scattering data were performed. Some improvement in the fit (not shown) was achieved ($\chi_\nu^2 = 3.0$) when the stalk was bent through an angle of 120° so that its new long-axis position was almost parallel to a chord between the centers of the catalytic cores. However, such an extreme bend seems improbable based on the above-mentioned shadowing work. In addition, the average intensity from a model in which the stalk beyond residue 375 pivoted through all Euler angles with equal probability (segmental flexibility) was computed. Although this model gave an improved fit (not shown) to the longest chords compared to the unmodified crystal structure model, a good fit to the overall scattering pattern was not achieved ($\chi_\nu^2 = 2.7$).

To understand what effect complete angular disordering (full segmental flexibility) of the catalytic cores might have on the observed scattering, we computed (Figure 6) the ensemble-averaged scattering pattern that would be obtained if both catalytic cores were allowed to randomly pivot through all (nondegenerate) orientations (six parameters). To eliminate the most severe overlap of the catalytic cores without the necessity of the introduction of extra parameters and additional computation, dimer models were included in the average only if $d_{\text{sep}} > 2.5$ nm. While this approximation is undoubtedly simplified, it does demonstrate what might be expected: the peak in the $P(r)$ function near 3 nm is increased somewhat while that near 6 nm is almost completely averaged out, and the overall fit is poor. Since the peak in the data near 6 nm (see Figure 5) is as strong relative to the peak near 3 nm as in the crystal structure $P(r)$, it seems unlikely that disordering would be the sole cause of the poor fit.

We found it more fruitful to reexamine the position of the catalytic cores within the rKIN379 model. For this purpose we searched the catalytic core positions in hKIN420 assuming only rigid-body rotations (see Experimental Procedures for details). The first model investigated used the crystallographically determined kinesin *monomer* structure of Sack et al. (*33*). We reasoned that since the monomer structure was obtained from a crystal different from that of

---

[5] Secondary structure predictions using COILS (*29*) indicate that for human kinesin there is a valley in the probability of finding an α-helix near 375, but beyond residue 405 the α-helix probability becomes high again.

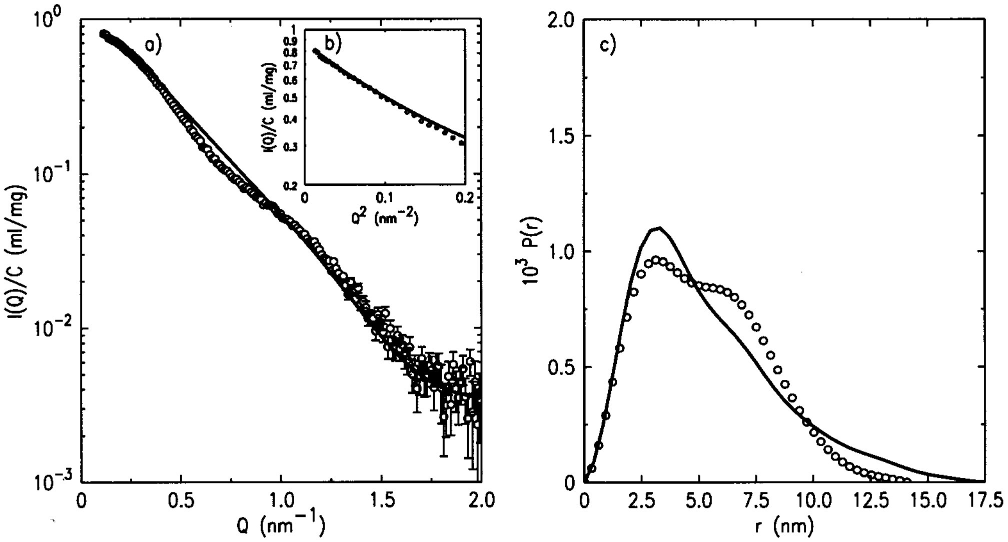

FIGURE 6: Expected average scattering from KIN420 dimers whose catalytic cores have complete segmental flexibility (a) Plot of observed intensity vs Q. The solid line was computed by averaging the scattering patterns from dimers generated as in Figure 5a but having all possible (nondegenerate) catalytic core orientations subject to the constraint that the cores had $d_{\text{sep}} > 2.5$ nm. This constraint minimized overlap of the catalytic cores with each other. The open circles are data as in Figures 1 and 5. Data and model are normalized at the lowest Q point. The scattering patterns used in the ensemble average were computed without correction for a solvent shell. (b) Guinier plot of the same data and model as in (a). (c) Chord distributions [$P(r)$] obtained by Fourier transforming the scattering data in (a) and the calculated ensemble-averaged scattering (solid line).

Table 2: Results of Modeling Kinesin Scattering with Crystallographic Dimers[a]

ϕ_1/ϕ_2 (deg)	θ_1/θ_2 (deg)	ψ_1/ψ_2 (deg)	θ_{neck} (deg)	d_{sep} (nm)	$R_g^{\text{in vacuo}}$ (nm)	R_g^{hydrated} (nm)	χ_ν^2
Identical Catalytic Core Orientation (Sack et al. Monomer), Only θ_{neck} Varies (One Parameter)							
0/0	0/0	0/0	107.5	5.29	4.27	4.50	2.75
One Catalytic Core Is As in Sack et al. Monomer, Other Catalytic Core Varies (Four Parameters)							
0/−30	0/65	0/−32.5	170	5.29	4.15	4.37	2.10
Strict 2-fold Symmetry about Rod Axis with Identical Catalytic Core Orientation (Three Parameters)							
110/110	60/60	137.5/137.5	180	5.57	3.86	4.08	1.94
Identical Catalytic Core Orientation except No 2-fold Symmetry (Four Parameters)							
90/90	42.5/42.5	205/202.5	117.5	5.35	3.94	4.10	1.22
Each Catalytic Core Pivots Independently about 2-fold Symmetry-Related Pivot Points (Six Parameters)							
70/142.5	45/97.5	200/180	180	5.23	3.91	4.08	1.11

[a] All calculations were done with missing residues in the catalytic cores of the crystal structure readded with half placed at each end of the known portion of the loop. The results were negligibly different when loop 11 of ref *6* was readded or there were no readditions.

the dimer structure, it might yield a better fit. This monomer structure contains a short run of single α-helix belonging to the neck, and the entire monomer can be approximately aligned with one of the catalytic cores in the rKIN379 dimer structure (*13*). After splicing the first of these cores onto the neck by aligning the α-helical portions, the position of the second was fit by allowing the polar angle (θ_{neck}) between the first and second catalytic cores to vary. The best fit orientation ($\theta_{\text{neck}} = 107.5°$; see Table 2) gave an improvement over the crystallographic-based dimer structure and reduced the χ_ν^2 from 5.2 to 2.75. In a related second model (Table 2), one of the catalytic cores was a Sack et al. monomer held fixed in the spliced position, and the other catalytic core (initially also a Sack et al. monomer) was allowed to rotate through all possible Euler angles about the Thr^{338} pivot point as well as through all possible θ_{neck}. This improved the fit somewhat ($\chi_\nu^2 = 2.1$). Replacement of the spliced-on Sack et al. monomer by either of the catalytic cores from the dimer crystallographic structure (3KIN) in the above two models produced no significant change in the quality of the fits (not shown).

Another model (third entry in Table 2), in which the dimer catalytic cores were allowed to take any orientation about the pivot point but were forced to have 2-fold symmetry, produced a marginally better fit than the second model in Table 2. A significant improvement in the quality of the fit could be achieved when the 2-fold symmetry about the neck axis was relaxed. It was then possible to achieve statistically good fits either by rotating each catalytic core though identical Euler angles ($\chi_\nu^2 = 1.22$, fourth entry in Table 2, data not shown), or by rotating each catalytic core independently about the (symmetrically related) pivot points ($\chi_\nu^2 = 1.11$, last entry in Table 2, Figure 7). The mass distributions and overall appearances in these two cases are quite similar, although the catalytic core domains differ in orientation. The results for the last three models, which used dimer catalytic cores, were independent of which catalytic core was used as a starting model. We conclude that for kinesin dimers a 2-fold symmetry axis, like that observed for *ncd*, is untenable.

In fitting scattering patterns, one must be concerned about the uniqueness of any modeling because of limited information content of the data. As the number of parameters

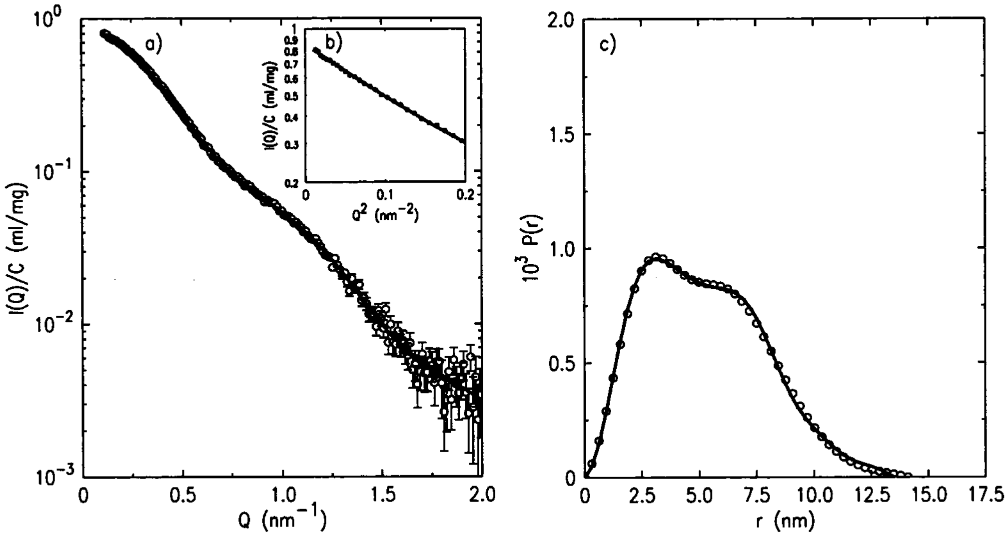

FIGURE 7: Fits to hKIN420 X-ray scattering by a model in which catalytic cores are allowed to pivot independently about symmetry-related pivot points (last entry in Table 2). (a) Plot of observed intensity vs *Q*. The solid line is the best-fitting modeling result. (b) Guinier plot of the same data and model as in (a). (c) Chord distributions [*P*(*r*)] obtained by Fourier transforming the scattering data in (a) and the calculated scattering by the best-fitting model (solid line).

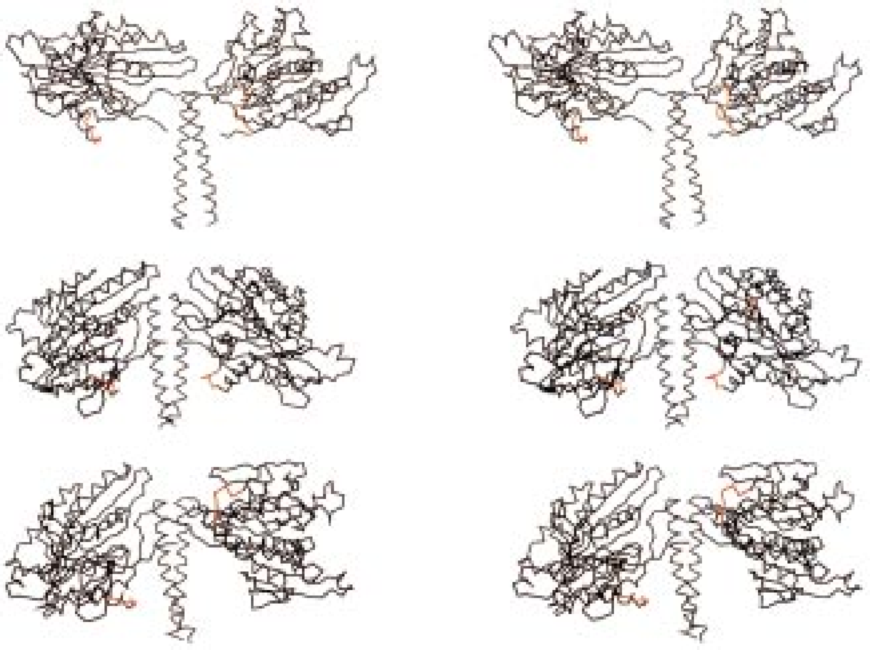

FIGURE 8: Models of the kinesin dimer structure. In these stereoviews the necks are aligned vertically and loop 12 is shown (red) on each catalytic core. The stalk portions (beyond residue 370) have been deleted for display purposes. (Top) Crystal structure (3KIN) of rKIN379. (Middle) Best-fit model of hKIN420 obtained with identical catalytic core orientations but no 2-fold symmetry about the rod axis (the next-to-last entry in Table 2). (Bottom) Best-fit model of hKIN420 obtained with each catalytic core pivoting independently about 2-fold symmetry-related pivot points (the last entry in Table 2). The fit to the data is shown in Figure 7.

describing the model increases, the likelihood that a model is unique decreases. Generally, we have found that for a given model the fitting was robust and converged to the same final orientation independent of starting orientation. In one instance we found a shelf in parameter space which gave a statistically plausible ($\chi_\nu^2 \approx 1.3$) fit. This shelf was observed in a fit that eventually converged to $\chi_\nu^2 = 1.11$ (the last entry in Table 2). However, this model was discarded as untenable because of the large overlap of one catalytic core with the neck portion.

Figure 8 shows the rKIN379 crystal structure, the model having identical rotation of the catalytic cores (fit in Figure 6) and the model in which the catalytic cores independently rotate about the symmetric pivot points model (fit in Figure 7). Although the lack of 2-fold symmetry about the neck axis is retained in these models, their overall appearance differs somewhat from the crystal structure. Viewed side-on, the “T”-like (or even slightly “Y”-like) appearance of the crystallographic structure is replaced by something more nearly resembling the projection of a mushroom. The orientation of the putative microtubule binding site (loop 12, residues 273−278 of hKIN) determined by alanine scanning mutagenesis (*34*) is now somewhat different in the two models from those of the crystal structure—particularly in the best-fitting model (Figure 8, bottom).

DISCUSSION

We have found that the structure of NCD281 in solution is well described by the crystal structure plus missing residues in the stalk and catalytic core domain despite some uncertainty about how to readd the missing residues in the catalytic core. In addition, scattering by the longer constructs, NCD250 and NCD224, is well fit at low Q by similar models having longer rigid coiled-coil stalks. Kinesin, on the other hand, is not well fit by the rKIN379 crystal structure plus missing residues. This poor fit is not due to missing residues in the catalytic core domain, as the number of such residues is small. The measured R_g (4.05 ± 0.075 nm) is much smaller than the prediction from the crystal-structure-based model ($R_g^{\text{hydrated}} = 4.63$ nm). Modeling of wide-angle data indicates that the separation of the catalytic cores is 0.7−1 nm smaller than in the crystallographic structure. Although we cannot rule out some contribution of bending of the stalk to the lack of agreement between the crystal-based structure and the data, it is unlikely to be the sole source.

We note that the models employed here do not take into account intramolecular disorder but rather assume a monodisperse ensemble of independent scatterers. However, in general, solution scattering reports an ensemble average of the shapes of the scatterers. Thus, if there is large-scale disorder, such as segmental flexibility of the kinesin catalytic cores as found for the head (S1) moieties of myosin (*35*), the modeling of the data by simple static structures is approximate. As discussed above, our scattering data indicated that the catalytic cores are not fully disordered. Evidence has been presented for some flexibility in fluorescence depolarization experiments using mant-nucleotide fluorophores bound to dimeric kinesin (*31*). There, the ratio of the observed rotational correlation time of the kinesin dimer to the kinesin monomer is 3.5−5.5. (For myosin this ratio is near 2.) If the catalytic core domain contained a completely immobile fluorophore, and the catalytic core domain of kinesin were a rigid body loosely tethered by a long chain to the remainder of a very large body, this ratio would be 1. Thus, the fluorescence depolarization data also indicate that there is a significant restriction of the rotational mobility of the catalytic core domain in the dimer. However, at present it is difficult to quantitatively estimate the degree of restriction, and this issue remains an open question.

Since scattering data do not give atomic resolution information, it is difficult to reliably assign core−core or interchain core−neck interactions for kinesin. While it is tempting to assign a source of core−core interactions to interactions between N-terminal residues or interchain core−neck interactions to N-terminal−neck residues, there could be other interactions near the top of the structure (as viewed in Figure 8) or further down along the neck. For example, the putative microtubule binding site (loop 12; cyan in Figure 8) of one catalytic core might interact in a switch-like fashion with residues on the rod (see particularly Figure 8, bottom structure). Such bonds could be either weak or strong. However, core−core interactions and/or interchain core−neck interactions would have to dominate intrachain interactions in order to break the 2-fold symmetry otherwise imposed by the parallel coiled-coil neck.

The nature of the binding of kinesin dimer constructs to microtubules has recently been a source of considerable controversy. Three-dimensional image reconstructions of kinesin dimer constructs bound to microtubules originally indicated that one kinesin catalytic core was bound and one was free and partially disordered (*10*, *36*). This view has recently been challenged by new binding studies measuring the stoichiometry of kinesin dimers to $\alpha-\beta$ tubulin in microtubules (*37*) as well as supporting STEM, cross-linking, scattering, and imaging studies (*37*, *38*). These more recent results indicate that each catalytic core domain binds identically to $\alpha-\beta$ tubulin dimers and that the mass assigned previously to the free catalytic core may actually arise from a portion of the neck of kinesin. At the same time others (*28*), using the original interpretation of three-dimensional image reconstructions, have suggested how the crystallographic kinesin dimer structure can be fit into cryo-EM density maps of kinesin dimers bound to microtubules. This fitting indicates that the microtubule binding site of kinesin is located on the side of the catalytic core domain opposite from that found by alanine scanning mutagenesis (*34*). The somewhat different views of the kinesin dimer structure presented herein admit that fits to EM data using the original interpretation may be possible without conflicting with the results of the alanine scanning. Alternatively, it is possible that the fitting by Kozielski et al. may have been fortuitous. We are currently investigating this issue. However, we note that alignment of the left-most core of either of the two best-fitting models with the left-most core of 3KIN (in Figure 8) indicates that the coiled-coil neck portion seems to more easily clear the surface of MTs (see *39*) if we assume that the left-most head binds in the original monomer (*11*, *12*, *34*) orientation. The second (presumably unbound) head will be somewhat more steeply inclined to the neck axis so that the cores will form arrowheads pointing approximately in the plus direction. The lack of 2-fold symmetry seen here (and in the crystal structure) suggests that location of the unbound head near an upstream binding site, as seen in the earlier electron microscopy, is a property of the structure of the free kinesin−ADP dimer. Further large-scale conformational changes may not be needed to achieve the bound state seen by electron microscopy.

In summary, the scattering results presented here show that the crystallographic structure of the *ncd* dimer is close to that which would be found during the part of the ATPase cycle when *ncd* (with bound ADP) is detached from microtubules and free in solution. The kinesin dimer solution structure does not fit the crystallographic structure (when stalk residues are added). The most likely cause of this discrepancy is that the catalytic cores are closer together and oriented somewhat differently in solution. Nevertheless, some of the central differences between *ncd* and kinesin dimers found by crystallography are retained. The catalytic cores in kinesin are not tightly bound to the neck, and their orientation lacks 2-fold symmetry about the rod axis. In *ncd* dimers the situation is reversed. This major structural difference between *ncd* and kinesin may be associated with the difference in the directionality of their movement (*5*) on microtubules and the ability of kinesin, but not *ncd*, to exhibit processivity (*40*).

ACKNOWLEDGMENT

We thank Ms. I. Krylova for able biochemical assistance and Drs. H. Tsuruta and T. Slawecki for helpful beamline assistance. We thank Ms. Kyra Oswald for help with collecting X-ray scattering data. We are indebted to Dr. E. Sablin for the gift of the *ncd* clones and Dr. R. Vale for the gift of the kinesin clone. We thank Dr. D. Svergun for helpful discussions about his programs. R.A.M. gratefully acknowledges many helpful and stimulating conversations with Dr. R. Fletterick. Work was done partially at SSRL, which is funded by the DOE OBES, by the DOE OHER, and by the NIH BRTP, Division of Research Resources. We acknowledge the support of the National Institute of Standards and Technology, DOC, in providing some of the neutron research used in this experiment. This work benefited from the use of the Low-*Q* Diffractometer at the Manuel Lujan, Jr., Neutron Scattering Center, Los Alamos National Laboratory, and was funded by the DOE (7405-ENG-36 with the University of California). This work was conducted under the auspices of the DOE, supported (in part) by funds provided by the University of California for the conduct of discretionary research by Los Alamos National Laboratory. We acknowledge use of the UCSF Computer Graphics Laboratory, which is supported by NIH Grant RR-01081.

REFERENCES

1. Vale, R. D., and Fletterick, R. J. (1997) *Annu. Rev. Cell Dev. Biol. 13*, 745−777.
2. Block, S. M. (1998) *Cell 93*, 5−8.
3. Inoue, Y., Toyoshima, Y. Y., Iwane, A. H., Morimoto, S., Higuchi, H., and Yanagida, T. (1997) *Proc. Natl. Acad. Sci. U.S.A. 94*, 7275−7280.
4. Tripet, B., Vale, R. D., and Hodges, R. S. (1997) *J. Biol. Chem. 272*, 8946−8956.
5. Sablin, E. P., Case, R. B., Dai, S. C., Hart, C. L., Ruby, A., Vale, R. D., and Fletterick, R. J. (1998) *Nature 395*, 813−816.
6. Kull, F. J., Sablin, E. P., Lau, R., Fletterick, R. J., and Vale, R. D. (1996) *Nature 380*, 550−555.
7. Sablin, E. P., Kull, F. J., Cooke, R., Vale, R. D., and Fletterick, R. J. (1996) *Nature 380*, 555−559.
8. Lockhart, A., and Cross, R. A. (1994) *EMBO J. 13*, 751−757.
9. Shimizu, T., Toyoshima, Y. Y., Edamatsu, M., and Vale, R. D. (1995) *Biochemistry 34*, 1575−1582.
10. Arnal, I., Metoz, F., DeBonis, S., and Wade, R. H. (1996) *Curr. Biol. 6*, 1265−1270.
11. Sosa, H., Dias, D. P., Hoenger, A., Whittaker, M., Wilson-Kubalek, E., Sablin, E., Fletterick, R. J., Vale, R. D., and Milligan, R. A. (1997) *Cell 90*, 217−224.
12. Hirose, K., Cross, R. A., and Amos, L. A. (1998) *J. Mol. Biol. 278*, 389−400.
13. Kozielski, F., Sack, S., Marx, A., Thormahlen, M., Schonbrunn, E., Biou, V., Thompson, A., Mandelkow, E. M., and Mandelkow, E. (1997) *Cell 91*, 985−994.
14. Fujiwara, S., Kull, F. J., Sablin, E. P., Stone, D. B., and Mendelson, R. A. (1995) *Biophys. J. 69*, 1563−1568.
15. Studier, F. W., Rosenberg, A. H., Dunn, J. J., and Dubendorff, J. W. (1990) *Methods Enzymol. 185*, 60−89.
16. Case, R. B., Pierce, D. W., Hom-Booher, N., Hart, C. L., and Vale, R. D. (1997) *Cell 90*, 959−966.
17. White, H. D. (1982) *Methods Enzymol. 85 (Part B)*, 698−708.
18. Gill, S. C., and von Hippel, P. H. (1989) *Anal. Biochem. 182*, 319−326.
19. Mendelson, R. A., Schneider, D. K., and Stone, D. B. (1996) *J. Mol. Biol. 256*, 1−7.
20. Tsuruta, H., Brennan, S., Rek, Z. U., Irving, T. C., Tompkins, W. H., and Hodgson, K. O. (1998) *J. Appl. Crystallogr. 31*, 672−682.
21. Hjelm, R. P. (1988) *J. Appl. Crystallogr. 21*, 618−628.
22. Goldstein, H. (1950) *Classical Mechanics*, Addison-Wesley Press, Cambridge, MA.
23. Svergun, D., Barberato, C., and Koch, M. H. J. (1995) *J. Appl. Crystallogr. 28*, 768−773.
24. Svergun, D. I., Richard, S., Koch, M. H., Sayers, Z., Kuprin, S., and Zaccai, G. (1998) *Proc. Natl. Acad. Sci. U.S.A. 95*, 2267−2272.
25. Svergun, D. I., Semenyuk, A. V., and Feigin, L. A. (1988) *Acta Crystallogr. A44*, 244−250.
26. Jiang, W., Stock, M. F., Li, X., and Hackney, D. D. (1997) *J. Biol. Chem. 272*, 7626−7632.
27. Moore, P. B. (1980) *J. Appl. Crystallogr. 13*, 168−175.
28. Kozielski, F., Arnal, I., and Wade, R. H. (1998) *Curr. Biol. 8*, 191−198.
29. Lupas, A. (1996) *Methods Enzymol. 266*, 513−525.
30. Thormahlen, M., Marx, A., Sack, S., and Mandelkow, E. (1998) *J. Struct. Biol. 122*, 30−41.
31. Rosenfeld, S. S., Correia, J. J., Xing, J., Rener, B., and Cheung, H. C. (1996) *J. Biol. Chem. 271*, 30212−30221.
32. Hirokawa, N., Pfister, K. K., Yorifuji, H., Wagner, M. C., Brady, S. T., and Bloom, G. S. (1989) *Cell 56*, 867−878.
33. Sack, S., Muller, J., Marx, A., Thormahlen, M., Mandelkow, E. M., Brady, S. T., and Mandelkow, E. (1997) *Biochemistry 36*, 16155−16165.
34. Woehlke, G., Ruby, A. K., Hart, C. L., Ly, B., Hom-Booher, N., and Vale, R. D. (1997) *Cell 90*, 207−216.
35. Mendelson, R. A., Morales, M. F., and Botts, J. (1973) *Biochemistry 12*, 2250−2255.
36. Hirose, K., Lockhart, A., Cross, R. A., and Amos, L. A. (1996) *Proc. Natl. Acad. Sci. U.S.A. 93*, 9539−9544.
37. Thormahlen, M., Marx, A., Muller, S. A., Song, Y., Mandelkow, E. M., Aebi, U., and Mandelkow, E. (1998) *J. Mol. Biol. 275*, 795−809.
38. Hoenger, A., Sack, S., Thormahlen, M., Marx, A., Muller, J., Gross, H., and Mandelkow, E. (1998) *J. Cell Biol. 141*, 419−430.
39. Romberg, L., Pierce, D. W., and Vale, R. D. (1998) *J. Cell Biol. 140*, 1407−1416.
40. Crevel, I. M., Lockhart, A., and Cross, R. A. (1997) *J. Mol. Biol. 273*, 160−170.

BI982374Z